

Tomographic laser absorption spectroscopy using Tikhonov regularization

Avishek Guha¹ and Ingmar Schoegl^{2, *}

¹*Merchant Gases R&D, Air Products and Chemicals Inc., Allentown, PA 18195, USA*

²*Mechanical & Industrial Engineering Department,
Louisiana State University, Baton Rouge, LA 70803, USA*

compiled: November 5, 2018

The application of tunable diode laser absorption spectroscopy (TDLAS) to flames with non-homogeneous temperature and concentration fields is an area where only few studies exist. Experimental work explores the performance of tomographic reconstructions of species concentration and temperature profiles from wavelength-modulated TDLAS measurements within the plume of an axisymmetric McKenna burner. Water vapor transitions at 1391.67 nm and 1442.67 nm are probed using calibration free wavelength modulation spectroscopy with second harmonic detection (WMS- $2f$). A single collimated laser beam is swept parallel to the burner surface, where scans yield pairs of line-of-sight (LOS) data at multiple radial locations. Radial profiles of absorption data are reconstructed using Tikhonov regularized Abel inversion, which suppresses the amplification of experimental noise that is typically observed for reconstructions with high spatial resolution. Based on spectral data-reconstructions, temperatures and mole fractions are calculated point-by-point. Here, a least-squares approach addresses difficulties due to modulation depths that cannot be universally optimized due to a non-uniform domain. Experimental results show successful reconstructions of temperature and mole fraction profiles based on two-transition, non-optimally modulated WMS- $2f$ and Tikhonov regularized Abel inversion, and thus validate the technique as a viable diagnostic tool for flame measurements.

1. Introduction

Over the last couple of decades, a significant amount of work has been performed in the area of temperature and species concentration determination using tunable diode laser absorption spectroscopy [1–4]. Line-of-sight TDLAS signals are, in essence, attenuation that is integrated along the beam path. Hence, these techniques, – while good for domains with uniform temperature and species concentration, – are not readily applicable for areas where the fields vary significantly. For such cases, the application of tomography along with TDLAS provides a means to achieve spatially resolved beam attenuation data which can be subsequently used for the determination of temperature and concentration values.

Tomographic TDLAS, for 1D tomography in particular, is generally achieved by acquiring LOS attenuation data, – i.e. projections, – using a parallel rake of rays scanned across an axisymmetric flame [5, 6]. Projections are subsequently deconvolved us-

ing a numerical implementation of Abel’s inversion equation [6–8]. Since Abel inversion is an inherently ill-conditioned problem [8, 9], small levels of measurement noise in projection data are amplified in the solution. Therefore, deconvolutions are usually performed for coarse grid spacing [8] and/or after artificial smoothing of projection data [5, 6].

Available work on tomographic TDLAS falls into two categories: tomography of axisymmetric domains, – which is essentially 1D, – and reconstructions of 2D slices using projections from multiple directions/views. Another distinction can be made with respect to the number of spectral transitions being probed. Two important prior studies on 1D tomographic TDLAS are works by Silver et al. [5] and Villarreal and Varghese [6]. Both studies use traditional Abel inversion to deconvolve LOS data and use relatively large beam spacing. While the experimental setup of the present study is a variation of the one used by Villarreal and Varghese [6], the previous study used 9 spectral transitions to simultaneously reconstruct temperature and concentration profiles using a scanned direct absorption method. Silver et al. [5] used WMS- $2f$ to re-

* Corresponding author: ischoegl@lsu.edu

construct concentration profiles of H_2O for a flame in microgravity. While this approach is nominally similar, the previous study decoupled measurements by a semi-computational approach: concentrations are found directly from lines with low temperature sensitivity, whereas corresponding temperatures are calculated. The present work, however, determines concentration (mole fractions) and temperature simultaneously and furthermore seeks to augment the performance of highly resolved Abel inversion by the introduction of Tikhonov regularization. An alternative approach is hyperspectral tomography, which was introduced in the context of 2D reconstructions [10–14]. In this method, LOS absorbance data are obtained for a large number of spectral transitions using a broadly tunable diode laser. The strength of this method is that the redundancy of spectral information allows for a reduction of views for a satisfactory reconstruction. Furthermore, recent proof-of-concept computational work indicates that hyper-spectral LAS methods can be combined with WMS-2f [15]. Hyper-spectral methods require frequency-agile lasers that allow for broadband modulation. In 1D tomography, the redundancy of spectral information is less critical; as will be shown, a small number of inexpensive laser diodes with narrow modulation capability is sufficient.

The goal of this study is to produce high resolution 1D reconstructions using Tikhonov regularized Abel inversion with two-transition WMS-2f TD-LAS, where experimental validations are performed for an axisymmetric McKenna burner. WMS-2f for species measurements dates back to at least the early 1990’s [1, 5, 16] and has found application in a range of recent studies [17–20]. Compared to direct absorption (DA) spectroscopy, WMS-2f has the advantage of producing a significantly higher signal-to-noise ratio. This is achieved by detecting the harmonics at frequencies that are high enough to reject much of the low-frequency high-amplitude relative intensity noise [20, 21] that are typical in diode lasers. From an experimental point of view, WMS-2f is advantageous [22, 23] since the first harmonic signal can be used as an effective tool for normalizing any variation of the second harmonic signal (calibration-free) [19, 23] for optically thin samples. This approach is attractive, as it eliminates low-frequency noise and makes measurement independent of signal disturbances due to window fouling or beam walking. Since temperature and concentration vary significantly within the domain, modulation depths for WMS-2f cannot be universally opti-

mized as is commonly done for homogeneous media [17, 20]. Instead of a two-transition ratio technique with optimal modulation depths, temperature and mole fractions are simultaneously determined by using a Levenberg-Marquardt least squares algorithm with non-optimal modulation depths.

2. Theory

A wavelength-modulated laser beam passing through a non-uniform temperature and concentration field is subject to path-integrated beam attenuation. The resulting signal can be deconvolved using traditional tomographic methods to produce local contributions to the beam attenuation. These values are then used to calculate temperature and mole fraction via a two-transition WMS-2f method. The following sections summarize the theory behind WMS-2f thermometry and detail Tikhonov regularized Abel inversion of data derived from WMS-2f.

2.A. Wavelength Modulation Spectroscopy

For a monochromatic beam passing through an absorbing medium, Beer-Lambert’s law relates the incoming (I_0) and transmitted (I_t) intensity at wavelength ν as

$$\left(\frac{I_t}{I_0}\right)_\nu = \exp(-\alpha(\nu)) = \tau(\nu) \quad (1)$$

Here, τ is the transmission coefficient while α is the absorbance. For uniform temperature and concentration, the absorption due to a single species is

$$\alpha(\nu) = PXL \sum_i S_i(T) \phi_i(\nu, X) \quad (2)$$

where P is the pressure, X is the mole fraction of the absorbing species, L is the total path length, S_i is the temperature dependent line-strength of the i -th transition, and ϕ_i is the corresponding Voigt lineshape function.

In WMS-2f experiments, a targeted absorption transition is scanned using a tunable diode laser, generally by a low frequency sawtooth ramp ($f_s \approx 1$ kHz) superimposed with a high frequency modulation ($f \approx 150 - 200$ kHz). The resulting instantaneous laser frequency is given by

$$\nu(t) = \bar{\nu}_s(t) + a \cos(\omega t) \quad (3)$$

Here, $\bar{\nu}_s(t)$ is the slowly ramping central laser wavelength, whereas a and $\omega = 2\pi f$ are modulation amplitude and angular frequency of laser frequency modulation (FM), respectively. In the following, $\theta = \omega t$ is introduced for convenience, and the slowly

varying $\bar{\nu}_s(t) \approx \bar{\nu}$ is considered constant with respect to the rapid modulation due to $f_s \ll f$.

Because of the modulation in wavelength, the instantaneous value of the transmission coefficient can be expressed as a periodic even function (or a cosine series) in θ , which takes the form

$$\tau(\nu(t)) = \tau(\bar{\nu} + a \cos \theta) = \sum_{k=0}^{\infty} H_k \cos k\theta \quad (4)$$

Here, the coefficients H_k for the k -th harmonic ($k = 0, 1, 2, \dots$) are found as

$$H_k = \frac{1}{n\pi} \int_{-\pi}^{+\pi} \tau(\bar{\nu} + a \cos \theta) \cos k\theta d\theta \quad (5)$$

where $n = 2$ if k is zero and $n = 1$ otherwise.

Under the assumption of an optically thin transition (i.e. $\alpha(\nu) < 0.1$ [19]), Eq. 1 is linearized as $\tau(\nu) \approx 1 - \alpha(\nu)$. Substituting into Eq. 5 yields

$$H_k = PXL \sum_i S_i(T) \Phi_{ik}(X) \quad (6a)$$

with line-shape integrals Φ_{ik} defined as

$$\Phi_{ik}(X) = -\frac{1}{n\pi} \int_{-\pi}^{+\pi} \phi_i(\nu(\bar{\nu}, a, \theta), X) \cos k\theta d\theta \quad (6b)$$

In general, Φ_{ik} are relatively insensitive to composition if an appropriate modulation depth a is chosen. For moderate ($\pm 10\%$) variations of concentration, a modulation amplitude a close to 2.2 half-widths of the transition yields almost constant Φ_{ik} [17, 20]. However, this property cannot be used in the context of tomography.

For the general case where gas composition and temperature vary along the line of sight L , the path-integrated harmonic coefficients are rewritten as

$$H_k = \int_0^L h_k(T(\ell), X(\ell)) d\ell \quad (7a)$$

where the local contribution to LOS values are

$$h_k(T, X) = P X \sum_i S_i(T) \Phi_{ik}(X). \quad (7b)$$

Equation 7 illustrates that individual harmonics in WMS-2f are path-integrated quantities, and thus can be deconvolved using conventional tomography. It is, however, noted that the assumption of an optically thin medium is essential to this approach.

2.B. Tomography of Spectroscopic Data

The deconvolution of path-integrated WMS-2f signals produces spectral data that are a function of local temperature and concentration. Here, Tikhonov

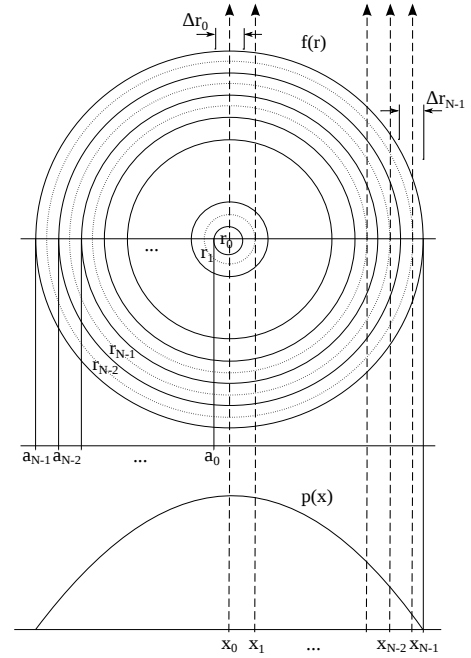


Figure 1: Domain discretization for Abel inversion.

regularized Abel inversion [9] addresses the inherent ill-conditioned nature of Abel inversion with closely packed rays. In the following, the concept is summarized for an arbitrary radially changing field variable $f(r)$ that result in projections $p(x)$. In the case of WMS-2f, these values correspond to linear combinations of local harmonics $h_k(T, X)$ and path-integrated measurements H_k at radial locations r , respectively. A detailed discussion of measured signals is given in Section 3.B.

For a numerical implementation of Abel inversion, an axisymmetric domain is subdivided into annular rings with rays passing through the center of each annulus as illustrated in Figure 1. Thus, rays x_0, x_1, \dots, x_{N-1} pass through annuli with labels a_0, a_1, \dots, a_{N-1} , respectively, where x_i correspond to radial distances r_i . With this definition of rays and annuli in place, the projection of field variables can be written as a sum of integrals over the whole domain as

$$p(x_m) = 2 \sum_{n=m}^{N-1} \int_{b_n}^{a_n} \frac{f(\tilde{r}) \tilde{r}}{(\tilde{r}^2 - r_m^2)^{1/2}} d\tilde{r} \quad (8a)$$

where the lower integration limit is

$$b_n = \begin{cases} r_n, & n = m \\ a_{n-1}, & n > m \end{cases}$$

If the field variable $f(r)$ is approximated by a Taylor series expansion around r_i , all integrals can be pre-calculated, where the Abel 3-point (ATP) scheme is

used [6, 8]. Thus, the system of analytical equations (Eq. 8a) is represented by

$$\mathbf{A}\mathbf{f} = \mathbf{p} \quad (8b)$$

where the vectors $\mathbf{f} = [f_0, f_1, \dots, f_{N-1}]^T$ and $\mathbf{p} = [p_0, p_1, \dots, p_{N-1}]^T$ contain discretized field variable values and projection values, respectively. The matrix \mathbf{A} acts as the *projection matrix*, where elements A_{mn} define the contribution of the n -th annulus to the projection value of the m -th ray.

Tikhonov regularization addresses the inherent ill-conditioning of the projection matrix \mathbf{A} [9, 24], which causes the amplification of measurement noise in the solution [8, 9]. Destabilization of reconstructed solution in highly resolved grids can be mitigated by augmenting the information by an additional set of equations

$$\lambda \mathbf{L}\mathbf{f} = \mathbf{0} \quad (9)$$

Here, λ is a parameter that controls the extent of regularization, whereas \mathbf{L} is used to penalize large gradients in the solution and is implemented as a discrete version of the ∇ operator, i.e.

$$\mathbf{L} = \begin{bmatrix} 1 & -1 & 0 & \dots & 0 \\ 0 & 1 & -1 & \dots & 0 \\ 0 & 0 & \dots & \dots & \dots \\ \dots & \dots & \dots & \dots & -1 \\ 0 & 0 & \dots & 0 & 1 \end{bmatrix}$$

Equations 8b and 9 form an overdetermined system, where a least-squares solution is sought as

$$\mathbf{f}_\lambda = \arg \min \left\{ \left\| \begin{bmatrix} \mathbf{A} \\ \lambda \mathbf{L} \end{bmatrix} \mathbf{f} - \begin{bmatrix} \mathbf{p} \\ \mathbf{0} \end{bmatrix} \right\| \right\} \quad (10)$$

Here, the regularization parameter λ controls the relative weight placed on accuracy and smoothness of the solution: a small λ value implies a solution that traces measurement points (including noise) accurately but may be highly oscillatory, whereas a large λ enforces a smooth solution that may deviate from measurements. While multiple methods for a proper choice of λ exist, this work adopts the *L-curve* criterion [24], which yields $\lambda \approx \mathcal{O}(1)$, and $\lambda = 1$ is used for all reconstructions.

3. Experimental Methods

3.A. Experimental Setup

Figure 2 shows the experimental setup that is used for 1D tomographic TDLAS of the post-flame zone of an axisymmetric McKenna burner (Holthuis & Associates). Spectroscopic data is generated by a pair of multiplexed laser beams tuned to transitions

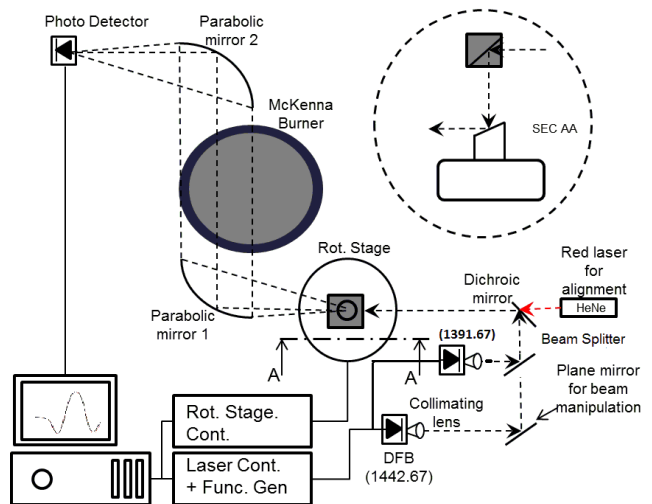


Figure 2: Experimental setup.

at 1391.67 nm and 1442.67 nm, respectively. The test section is probed by parallel rays, which are swept parallel to the burner surface with a setup consisting of a periscope mounted on a rotation stage and a single detector, both of which are positioned in the focal points of a pair of parabolic mirrors [6]. Injection currents and temperatures of both diode lasers (NLK1E5C1TA, NTT Electronics) are controlled by a dedicated controller (LDC-3908, ILX Lightwave). The temperature controller is used to set the central laser emission wavelength while the injection current is modulated using a programmed function generator (CG4340, Gagecard). The TO can diode lasers are collimated using an aspheric lens and shaped using an iris before being multiplexed in the time domain. The beam diameter is 0.5 mm, which also corresponds to the spatial resolution. The movement of a high-precision rotation stage (RGV-100 BL, Newport) is controlled by LabVIEW (National Instruments) to produce measurements in increments of 1mm. The raw signal from the photodetector (PDA-10CS, Thorlabs) is digitized using a digital oscilloscope (PCI-5105, National Instruments).

The function generator uses a 200Hz scanning ramp super-imposed with a 50 kHz sinusoidal modulation to create harmonics of the absorption signal. In measurements, sets of 10 sawtooth ramps (time-multiplexed, i.e. five per transition) are captured and passed individually through a digital lock-in-amplifier (implemented in software/LabVIEW). Harmonics of the modulated signal ($1f$ and $2f$) are written to a binary file for further post-processing. At each radial location, 100 data sets are obtained. Due to oversampling, a measurement at an indi-

vidual location takes 2 seconds per line. Modulation depths are chosen as 0.13 cm^{-1} and 0.1 cm^{-1} for transitions at 1442.67 nm and 1391.67 nm , respectively. The modulated laser output is validated using a Silicon etalon (Lightmachinery Inc.) with a free spectral range (FSR) of $\sim 0.017 \text{ cm}^{-1}$ in the $1.4 \mu\text{m}$ range.

Experiments use a methane/air McKenna flame with a nominal radius of 30 mm and an external shroud thickness of 7.5 mm . The burner produces a stationary flat flame, where equivalence ratios of 0.7 and 0.8 are tested for a mixture flow velocity of 20 cm/s . Tomographic measurements are taken 7 mm above the burner plate. Flow rates of methane and air are set by mass flow controllers (32907-71/32907-73, Cole-Parmer) using a LabVIEW interface. The flame is shielded by a nitrogen shroud flow, where the velocity is matched with the cold air-fuel mixture in order to minimize shear at the edge of the flame. The McKenna burner is supplied with cooling water at a rate of 800 ml/min , where the inlet temperature is held at 4°C by an enclosed ice bath.

3.B. Signal Processing

The non-ideal intensity modulation (IM) due to injection current modulation of a typical diode laser is modeled as [19, 25]

$$I_0(\theta) = \bar{I}_0 (1 + i_0 \cos(\theta + \psi_1) + i_2 \cos(2\theta + \psi_2)) \quad (11)$$

Here, \bar{I}_0 is the average incident laser intensity at $\bar{\nu}$, whereas i_0 and i_2 are normalized linear (1f) and non-linear (2f) modulation amplitudes, respectively. The corresponding phase shifts are given by ψ_1 and ψ_2 . Both are FM/IM phase shifts which gauge the lag between wavelength and intensity modulation.

In the following, the gas-attenuated raw detector signal is expressed in terms of instantaneous incident laser intensity and transmission coefficient as

$$I_t(\theta, \bar{\nu}, a) = GI_0(\theta) \tau(\bar{\nu} + a \cos \theta) \quad (12)$$

where G is the optical/electrical gain of the system.

In order to find the k -th overtone of the signal, the raw detector signal is passed through a digital lock-in-amplifier, where the detector signal is multiplied by reference signals (either $\cos(k\theta + \psi_d)$ or $\sin(k\theta + \psi_d)$) to produce x and y -components. Here, the detection phase shift ψ_d is the shift between intensity modulation and reference signal.

Traditionally, background subtracted lock-in-amplifier outputs are assessed as the vector sum of x and y components [19]. While this approach is independent of ψ_d , the resulting values are not linear combinations of harmonics and therefore cannot be

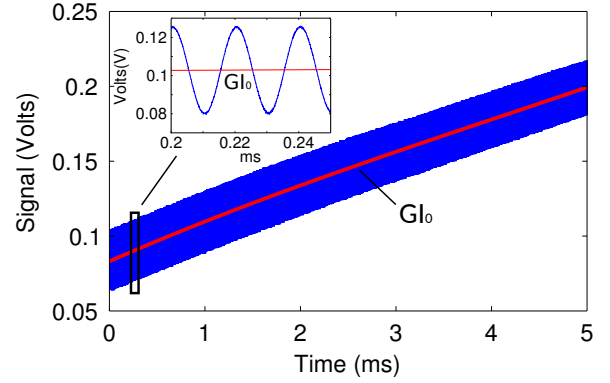


Figure 3: Raw detector signal used for laser characterization: raw signal for determination of i_0 .

used for tomography. In the present work, this issue is resolved by adjusting ψ_d to zero, which allows for traditional tomography based on the x -component of the signal alone. In the following, 1f and 2f outputs produced by the lock-in-amplifier are denoted by S_{1f} and S_{2f} , respectively.

It can be shown that both S_{1f} and S_{2f} are directly proportional to the instantaneous mean intensity of the laser [19]. The 1f signal is given by

$$S_{1f} = \frac{1}{2} G \bar{I}_0 i_0 (1 - f(P, X, L, T)) \approx \frac{1}{2} G \bar{I}_0 i_0 \quad (13)$$

where S_{1f} scales with laser intensity and 1f modulation amplitude under the assumption of optically thin samples where $f(P, X, L, T) \ll 1$. The calibration-free WMS-2f method uses this property to normalize the 2f signal by the 1f signal as

$$S_{2f}/S_{1f} = \frac{1}{i_0} [H_2 + \frac{1}{2} i_0 (H_1 + H_3) \cos \psi_1 + \dots + i_2 (1 + H_0 + \frac{1}{2} H_4) \cos \psi_2] \quad (14)$$

where H_k are defined in Eq. 7a.

In the absence of absorption, all H_k are zero, and the measured signal represents the background signal due to non-linearity of the diode laser, i.e.

$$S_{2f,0}/S_{1f} = \frac{i_2}{i_0} \cos \psi_2 \quad (15)$$

which is also known as residual amplitude modulation or RAM [19, 21, 26]. As $H_0, H_4 \ll 1$ in the optically thin limit, RAM is the leading order term among non-linear (2f) modulation effects. While RAM is usually neglected for small amplitudes of modulation [19], it has to be considered if signal strengths are of similar orders of magnitude.

3.C. Laser Characterization

In Equations 14 and 15, linear (i_0, ψ_1) and non-linear (i_2, ψ_2) modulation parameters are specific to the laser. Apart from spectroscopic data, measurements do not require further calibration once a laser diode is characterized.

In scanned WMS- $2f$, the injection current results from a high-frequency modulation that is superimposed on a low frequency ramp that determines the slowly varying center wavelength $\bar{\nu}$. In order to find i_0 , this output was normalized by the central detector output, which is found by fitting a 2nd order polynomial as shown in Fig. 3. The normalized linear amplitude i_0 is then found by performing a best-fit of a sinusoidal curve with the same frequency to the intensity signal and normalizing it with the average signal strength [19]. The linear FM/IM phase shift ψ_1 is determined by simultaneous monitoring of the output of two beam arms, where one is measured directly and the other is passed through an etalon.

Non-linear modulation effects due to i_2 and ψ_2 result in RAM (Eq. 15), which becomes non-negligible near the edge of the flame. In this work, RAM is considered, while higher-order non-linear modulation terms are neglected. In experiments, LOS signals are recorded without the presence of a flame and subtracted from measurements. In absence of absorption, this signal is equivalent to RAM. Absorption by ambient air is, however, non-negligible at 1391.67nm, where corrections account for both outside path length and RAM.

3.D. Tomographic TDLAS

In tomographic TDLAS, the output of the lock-in amplifier is recorded for two spectral transitions at multiple radial locations. Resulting spectroscopic data, – i.e. $(S_{2f} - S_{2f,0})/S_{1f}$ representing linear combinations of H_k , – are then deconvolved according to Equation 10. Thus, the deconvolved spectral data are linear combinations of $h_k(T, X)$ (Eq. 7b). In the following, deconvolved measurement data are referred to as $\zeta_j(T, X)$, where $j = 1, 2$ correspond to the two probed transitions.

In the context of tomography, variations of concentrations are not moderate, which means that line-shape-integrals (Eq. 6b) cannot be approximated as constants as commonly assumed in WMS- $2f$ [17, 20]. Instead, a Levenberg-Marquardt scheme with temperature and mole fraction as free parameters is adopted to account for non-ideal behavior.

Here, a variable Δ is defined as

$$\Delta(T, X) = \sqrt{\sum_{j=1,2} (\bar{\zeta}_j(T, X)/\zeta_j - 1)^2} \quad (16)$$

where $\bar{\zeta}_j(T, X)$ represent precalculated data for simulated measurements. Solutions for T and X are found by minimizing $\Delta(T, X)$ at each radial location using gradient-based optimization.

Simulated measurements are stored in a look-up-table, which contains spectral absorbance calculations for spectral data and gas composition of interest. Spectral parameters are based on HITRAN and HITEMP databases [27, 28], where transitions with line-strengths less than $10^{-34} \text{ cm}^{-1}/(\text{molecule cm}^{-2})$ are neglected. Simulated measurement data for $\bar{\zeta}_j(T, X)$ are obtained by taking a fast-Fourier transform (FFT) of the absorbance line shape around the transition line-centers where proper experimental values for a , i_0 and ψ_1 are substituted.

Uncertainties. Reconstructions are created based on 100 data sets per location, where each set contains 5 sawtooth scans per transition. For each sawtooth scan, WMS- $2f$ signals are processed and mean values and standard variations are recorded. Uncertainties based on the standard variation ($\pm 1\sigma$) are propagated to uncertainties in $\zeta_i(T, X)$ via the Abel uncertainty equation [8]. The projection matrix for Tikhonov regularized Abel inversion is

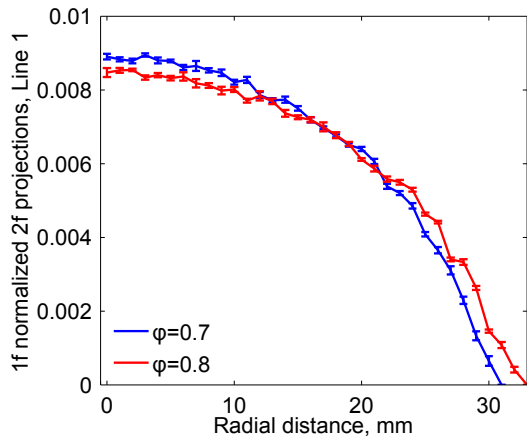
$$A^\# = (A^T A + \lambda^2 L^T L)^{-1} A^T \quad (17)$$

Uncertainty in $\zeta_j(T, X)$ are subsequently used to calculate the uncertainties in the temperature-mole fraction surface described by Eq. 16. Additional uncertainties due to mass-flow controllers ($\pm 2\%$) do not affect measurements directly, and thus are only of concern for the validation process.

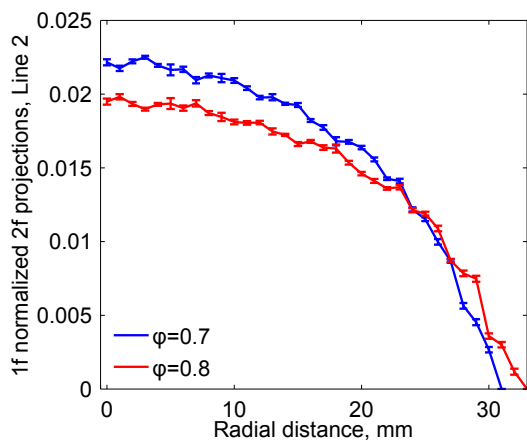
4. Results and Discussions

Tomographic reconstructions of radial temperature and mole fraction profiles are obtained for two specific cases, where equivalence ratios $\phi = 0.7$ and 0.8 , and a linear velocity of 20 cm/sec are chosen.

Individual Line Reconstructions. For tomographic measurements, spectroscopic data for both transitions are recorded at equispaced radial locations and passed through a digital lock-in amplifier with appropriately chosen detection phase ψ_d (Section 3.B). The S_{2f}/S_{1f} signal is formed (Eq. 14) and corrected for RAM (Eq. 15) and absorption outside the flame zone. The resulting data represent line-of-sight projection values, and are shown in Figures 4a and 4b. It is noted that small uncertainty levels



(a) Projection data at 1442.67 nm.

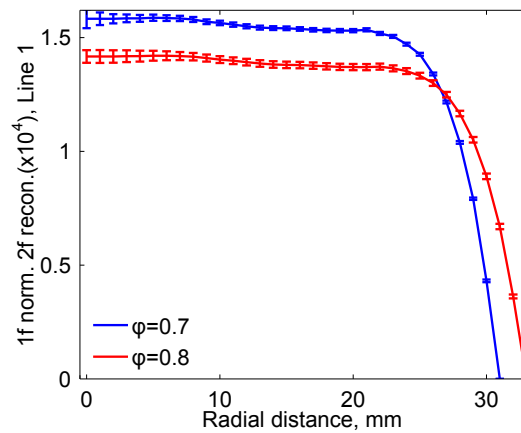


(b) Projection data at 1391.67 nm.

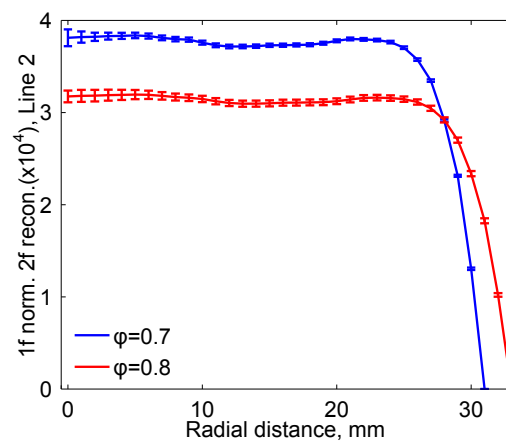
Figure 4: Projection data for spectral line measurements at $\phi = 0.7$ (blue) and 0.8 (red).

of measured projection values are due to noise rejection that is intrinsic to WMS-2f. Spectroscopic projection data are subsequently deconvolved using Tikhonov regularized Abel inversion (Eq. 10). The resulting distributions form $\zeta_j(T, X)$, which are $1f$ normalized $2f$ signal contributions per unit length within an axisymmetric domain.

Figures 5a and 5b show reconstructions of ζ_i distributions due to H_2O absorption at 1442.67 and 1391.67 nm, respectively. Results clearly show the expected behavior of a flat flame, i.e. a radial *top-hat* distribution. The central constant region is retrieved with good accuracy, whereas the lateral wings with rapidly decreasing values result from the interaction of the core region and the shroud flow. In measurements, non-zero absorption is observed outside the core zone, which is attributed to mixing as well as flow interactions due to thermal ex-



(a) Reconstructed profile at 1442.67 nm.

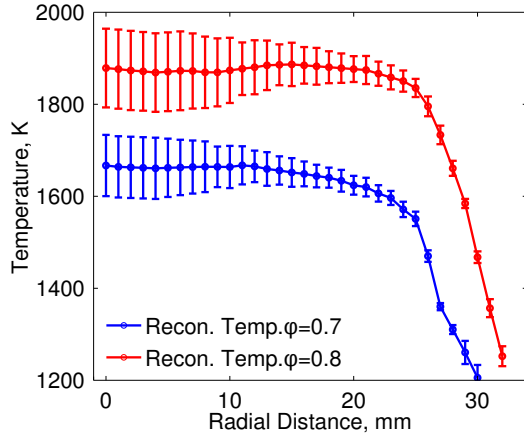


(b) Reconstructed profile at 1391.67 nm.

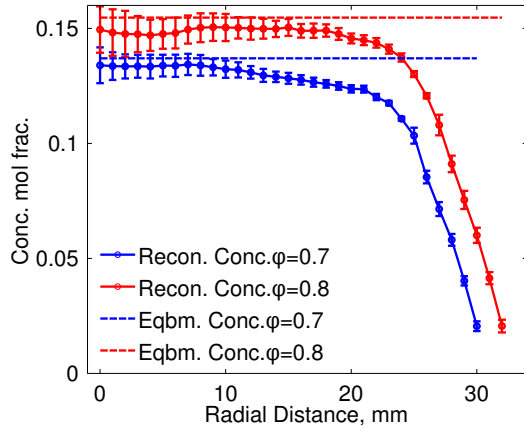
Figure 5: Reconstructed radial distributions of spectroscopic data at $\phi = 0.7$ (blue) and 0.8 (red).

pansion of reacting gases. This behavior was more pronounced for the higher equivalence ratio; accordingly, radial measurement domains are extended to 31 and 33 mm for $\phi = 0.7$ and 0.8, respectively. No flame interaction was detected at the outermost measurement point for either transition, i.e. the radial locations lie beyond the edge of the flame.

Temperature and Mole Fraction. Using individual line reconstructions, local temperature and water vapor mole fractions are reconstructed point-by-point using a Levenberg-Marquardt scheme (Eq. 16). Figures 6a and 6b show resulting radial profiles for temperature and mole fraction, respectively. Again, the expected top-hat profile is retrieved to good accuracy. Near the center, temperatures and vapor mole fraction at $\phi = 0.7$ are reconstructed as 1670K and 0.135 mol/mol, respectively. Corresponding values at $\phi = 0.8$ are 1900 K and 0.15



(a) Reconstructed temperature profiles.



(b) Reconstructed mole fraction profiles.

Figure 6: Temperature and mole fraction results with different values of ϕ .

mol/mol. Error bars are based on measurement uncertainty that is propagated through the tomographic reconstruction. Uncertainties near the center are around ± 70 K and ± 0.0077 mol/mol at $\phi = 0.7$, and almost ± 90 K and ± 0.01 mol/mol at $\phi = 0.8$. In Abel inversion, uncertainties are known to grow towards the center due to the intrinsic ill-posedness of the problem [9]. This is clearly reflected in results; uncertainty values are significantly smaller close to the edge of the flame.

Validation. Mole fractions of water vapor near the center of the flame are expected to be close to equilibrium mole fractions, regardless of parameters such as velocity of reactants, matrix material of the burner and cooling water flow rate and temperature [6, 29]. Results in Figure 6b illustrate that reconstructions near the center are within 1.5% and 4% of equilibrium values for $\phi = 0.7$ and 0.8, respec-

tively. The relative deterioration in mole fraction results for the higher equivalence ratio is attributed to a decreased sensitivity of the spectral line pair at higher temperatures.

In contrast to mole fraction values, reconstructed flame temperatures in burner stabilized flames are not suited for validation purposes, as they are always lower than adiabatic flame temperatures due to heat transfer from the flame zone to the burner plate. Experimental results are consistent, as adiabatic temperatures for $\phi = 0.7$ and 0.8 are 1839 K and 1997 K, respectively. Heat losses to the burner plate depend on a number of parameters, e.g. flame stabilization height, flow velocity, burning velocity, cooling water temperature and flow rates. Burner to burner temperature differences of the order of 25 K have been documented for otherwise identical experiments [29]; furthermore, results can be affected significantly by the burner material [30]. While a direct validation of temperature results is not justified, it is noted that for a given temperature and mole fraction, spectral absorbance and $2f$ heights are single valued within the temperature range of interest, i.e. reconstructions yield unique solutions. Therefore, a validation based on reconstructed mole fractions implies that temperatures are reconstructed within good accuracy.

5. Conclusions

This work focuses tomographic TDLAS based on a two-transition technique, which is an area where few studies exist. Within the optically thin limit, it is shown that WMS- $2f$ signals obtained from line-of-sight measurements represent path-integrated values. Thus, the $1f$ normalized $2f$ output of a lock-in amplifier can be deconvolved using traditional tomography; a variation of the three-point Abel algorithm is used to reconstruct profiles of absorption data for two H_2O transitions. Averaging of multiple scans in combination with Tikhonov regularization stabilizes the solution against detrimental effects of measurement noise, which is exacerbated by the proximity of the rays in traditional Abel inversion. Using reconstructions for two lines, a Levenberg-Marquardt optimization routine is adopted to solve simultaneously for unknown temperatures and mole fractions. This approach represents an extension of the WMS- $2f$ technique and can be easily extended to larger numbers of transitions. It is noted that traditional WMS- $2f$ approaches fail in the context of tomography, as line-shape integrals cannot be assumed to be constant. The experimental technique was validated in experiments, where reconstructions of temperature and mole fractions are in agreement

with the expected behavior.

Acknowledgments

This material is based upon work supported by the Louisiana Board of Regents Research Competitiveness Subprogram under contract number LEQSF(2010-2013)-RD-A-04. The authors thank Dr. Kyle Daun for valuable discussions and insights.

References

- [1] L. Philippe and R. Hanson, "Laser diode wavelength-modulation spectroscopy for simultaneous measurement of temperature, pressure, and velocity in shock-heated oxygen flows," *Appl. Opt.* **32**, 6090–6103 (1993).
- [2] X. Zhou, X. Liu, J. B. Jeffries, and R. K. Hanson, "Development of a sensor for temperature and water concentration in combustion gases using a single tunable diode laser," *Measurement Science and Technology* **14**, 1459 (2003).
- [3] X. Zhou, J. Jeffries, and R. Hanson, "Development of a fast temperature sensor for combustion gases using a single tunable diode laser," *Appl. Phys. B* **81**, 711–722 (2005).
- [4] A. Farooq, J. Jeffries, and R. Hanson, "CO₂ concentration and temperature sensor for combustion gases using diode-laser absorption near 2.7 μm ," *Appl. Phys. B* **90**, 619–628 (2008).
- [5] J. Silver, D. Kane, and P. Greenberg, "Quantitative species measurements in microgravity flames with near-ir diode lasers," *Appl. Opt.* **34**, 2787–2801 (1995).
- [6] R. Villarreal and P. Varghese, "Frequency-resolved absorption tomography with tunable diode lasers," *Appl. Opt.* **44**, 6786–6795 (2005).
- [7] N. Abel, "Auflösung einer mechanischen Aufgabe." *J. Reine Angew. Math.* **1826**, 153–157 (1826).
- [8] C. J. Dasch, "One-dimensional tomography: a comparison of abel, onion-peeling, and filtered backprojection methods," *Appl. Opt.* **31**, 1146–1152 (1992).
- [9] K. Daun, K. Thomson, F. Liu, and G. Smallwood, "Deconvolution of axisymmetric flame properties using Tikhonov regularization," *Appl. Opt.* **45**, 4638–4646 (2006).
- [10] L. Ma and W. Cai, "Determination of the optimal regularization parameters in hyperspectral tomography," *Appl. Opt.* **47**, 4186–4192 (2008).
- [11] L. Ma and W. Cai, "Numerical investigation of hyperspectral tomography for simultaneous temperature and concentration imaging," *Appl. Opt.* **47**, 3751–3759 (2008).
- [12] W. Cai, D. Ewing, and L. Ma, "Application of simulated annealing for multispectral tomography," *Comput. Phys. Commun.* **179**, 250–255 (2008).
- [13] L. Ma, W. Cai, A. W. Caswell, T. Kraetschmer, S. T. Sanders, S. Roy, and J. R. Gord, "Tomographic imaging of temperature and chemical species based on hyperspectral absorption spectroscopy," *Opt. Express* **17**, 8602–8613 (2009).
- [14] C. Hagen and S. Sanders, "Toward hyperspectral sensing in practical devices: Measurements of fuel, H₂O and gas temperature in a metal homogeneous charge compression ignition engine," *J. Near Infrared Spectrosc.* **15**, 217 (2007).
- [15] W. Cai and C. F. Kaminski, "Multiplexed absorption tomography with calibration-free wavelength modulation spectroscopy," *Appl. Phys. Letters* **104**, 154106 (2014).
- [16] J. A. Silver, "Frequency-modulation spectroscopy for trace species detection: theory and comparison among experimental methods," *Appl. Opt.* **31**, 707–717 (1992).
- [17] J. Liu, J. Jeffries, and R. Hanson, "Wavelength modulation absorption spectroscopy with 2f detection using multiplexed diode lasers for rapid temperature measurements in gaseous flows," *Appl. Phys. B* **78**, 503–511 (2004).
- [18] J. C. Liu, G. Rieker, J. Jeffries, M. Gruber, C. Carter, T. Mathur, and R. Hanson, "Near-infrared diode laser absorption diagnostic for temperature and water vapor in a scramjet combustor," *Appl. Opt.* **44**, 6701–6711 (2005).
- [19] H. Li, G. B. Rieker, X. Liu, J. B. Jeffries, and R. K. Hanson, "Extension of wavelength-modulation spectroscopy to large modulation depth for diode laser absorption measurements in high-pressure gases," *Appl. Opt.* **45**, 1052–1061 (2006).
- [20] A. Farooq, J. Jeffries, and R. Hanson, "Sensitive detection of temperature behind reflected shock waves using wavelength modulation spectroscopy of CO₂ near 2.7 μm ," *Appl. Phys. B* **96**, 161–173 (2009).
- [21] P. Kluczynski and O. Axner, "Theoretical description based on fourier analysis of wavelength-modulation spectrometry in terms of analytical and background signals," *Appl. Opt.* **38**, 5803–5815 (1999).
- [22] X. Liu, J. Jeffries, R. Hanson, K. Hinckley, and M. Woodmansee, "Development of a tunable diode laser sensor for measurements of gas turbine exhaust temperature," *Appl. Phys. B* **82**, 469–478 (2006).
- [23] G. B. Rieker, J. B. Jeffries, and R. K. Hanson, "Calibration-free wavelength-modulation spectroscopy for measurements of gas temperature and concentration in harsh environments," *Appl. Opt.* **48**, 5546–5560 (2009).
- [24] P. C. Hansen, *Rank-deficient and discrete ill-posed problems: numerical aspects of linear inversion*, vol. 4 (Society for Industrial Mathematics, 1987).
- [25] J. Reid and D. Labrie, "Second-harmonic detection with tunable diode lasers: Comparison of experiment and theory," *Appl. Phys. B* **26**, 203–210 (1981).

- [26] P. Kluczynski, Å. M. Lindberg, and O. Axner, "Background signals in wavelength-modulation spectrometry by use of frequency-doubled diode-laser light. ii. experiment," *Appl. Opt.* **40**, 794–805 (2001).
- [27] L. S. Rothman, I. E. Gordon, A. Barbe, D. C. Benner, P. F. Bernath, M. Birk, V. Boudon, L. R. Brown, A. Campargue, J.-P. Champion *et al.*, "The HITRAN 2008 molecular spectroscopic database," *J. Quant. Spectrosc. Radiat. Transfer* **110**, 533–572 (2009).
- [28] L. Rothman, I. Gordon, R. Barber, H. Dothe, R. Gamache, A. Goldman, V. Perevalov, S. Tashkun, and J. Tennyson, "HITEMP, the high-temperature molecular spectroscopic database," *J. Quant. Spectrosc. Radiat. Transfer* **111**, 2139–2150 (2010).
- [29] P. Weigand, R. Lückcrath, and W. Meier, "Documentation of flat premixed laminar CH₄air standard flames: Temperatures and species concentrations," Tech. rep., DLR Institute (2003).
- [30] F. Migliorini, S. De Iuliis, F. Cignoli, and G. Zizak, "How flat is the rich premixed flame produced by your McKenna burner?" *Combust. Flame* **153**, 384–393 (2008).